Magneto-optical properties of diluted magnetic PbSe/$Pb_{1-x}Mn_xSe$ superlattices

F. Geist and H. Pascher
Experimentalphysik I, Universität Bayreuth, D-95440 Bayreuth, Germany

M. Kriechbaum
Institut für Theoretische Physik, Universität Graz, A-8010 Graz, Austria

N. Frank and G. Bauer
Institut für Halbleiterphysik, Universität Linz, A-4040 Linz, Austria
(Received 19 January 1996; revised manuscript received 26 March 1996)

PbSe/$Pb_{1-x}Mn_xSe$ superlattices ($x<0.02$, periods: <40 nm) were grown by molecular-beam epitaxy on (111) oriented substrates. They were investigated by interband absorption in Faraday geometry ($\mathbf{B}\|\mathbf{k}\|[111]$) and by coherent anti-Stokes Raman scattering in the mid-infrared range with $\mathbf{B}\|[110]$ (i.e., in the plane of the layers) up to 7 T at temperatures in the range of 1.7–20 K. The latter method yields precise information on the spin splittings of valence and conduction bands as a function of applied magnetic field and of temperature. The experimental results yield a staggered band alignment with the conduction-band edge of the wider gap $Pb_{1-x}Mn_xSe$ layers below that of the PbSe layers. A detailed theoretical analysis is made on the basis of a four-band envelope-function approximation taking into account the exchange interaction between the localized electrons of the half-filled Mn^{2+} $3d$ shell and the mobile carriers in mean-field approximation. Energy eigenstates and eigenfunctions have been calculated as well as interband selection rules. For the Voigt geometry, where the electric and magnetic motions are not decoupled, the center coordinate of the Landau orbits remains a good quantum number, albeit that the corresponding degeneracy of eigenstates is lifted. The dependence of the eigenstates and of the g values on the value of the center coordinate along the superlattice growth direction is investigated in detail. A normalized conduction-band offset $\Delta E_c/\Delta E_g$ of -0.4 is obtained. [S0163-1829(96)10131-4]

I. INTRODUCTION

Among the IV–VI compound diode lasers, the ones based on PbSe and its ternary compounds, such as PbSe/$Pb_{1-x}Eu_xSe$ (Refs. 1–3) and PbSe/$Pb_{1-x}Sr_xSe$,[4] are of considerable importance in achieving tunable laser emission in the mid-infrared range. The partial replacement of Pb by Eu results not only in an increase of the energy gap[5] but also in interesting magnetic properties due to the half-filled $4f$ shell of the Eu^{2+} ions. Also, the transition metal manganese with a half-filled $3d$ shell increases the energy gap in the ternary compound $Pb_{1-x}Mn_xSe$ and shows in addition stronger magnetic interactions between the Mn^{2+} ions in comparison to $Pb_{1-x}Eu_xSe$.[6,7] Furthermore, magneto-optical interband investigations have revealed that the exchange interactions between the localized $3d$ electrons and the valence electrons are larger in $Pb_{1-x}Mn_xSe$ than those between the $4f$ electrons and the valence electrons in $Pb_{1-x}Eu_xSe$.[8–12]

In the range of Mn contents up to 3%, $Pb_{1-x}Mn_xSe$ has a band structure similar to PbSe, i.e., a minimum direct gap at the L points of the Brillouin zone with a mass anisotropy $K=m_l/m_t$ of about 2. The band parameters of PbSe and $Pb_{1-x}Mn_xSe$ were obtained by cyclotron resonance, interband magneto-optical investigations, and coherent anti-Stokes Raman scattering (CARS) experiments.[10,13,14] Recently, PbSe/$Pb_{1-x}Mn_xSe$ multiple-quantum-well and superlattice structures were grown by molecular-beam epitaxy[15] and investigated by absorption, modulated absorption, and photoconductivity measurements.[16] From these data it was inferred that in the range of compositions investigated, PbSe/$Pb_{1-x}Mn_xSe$ has a staggered band lineup with the conduction-band edge of the larger gap material ($Pb_{1-x}Mn_xSe$) lying below the conduction-band edge of the lower gap material (PbSe). Our preliminary magneto-optical interband and CARS experiments on PbSe/$Pb_{1-x}Mn_xSe$ corroborated these results on the band lineup.[17]

Diluted magnetic semiconductor superlattices with a staggered or a type-II band lineup are of particular interest for magneto-optical investigations, since electrons and holes are spatially separated from each other. Consequently, one carrier type is located in the layers with the magnetic ions, whereas the other one is spatially separated from the magnetic ions. The effect of the magnetic ions on the electrons and holes in $Pb_{1-x}Mn_xSe$ manifests itself in the different values of the g factors compared to PbSe. In the PbSe/$Pb_{1-x}Mn_xSe$ superlattices, consequently, the leakage of the carrier wave functions into the adjacent nonmagnetic layers (for the electrons) or magnetic layers (for the holes) has markedly different consequences for the effective g factors of electrons and holes. A detailed experimental and theoretical study of these effects is the purpose of this paper. In particular, CARS experiments are most suitable for the investigation of staggered diluted magnetic semiconductors, since, due to the presence of photoexcited minority carriers, spin-flip transitions involving electron *and* hole states are measured simultaneously in one experiment.

This paper is organized as follows. In Sec. II, a brief

TABLE I. Sample parameters of the PbSe/$Pb_{1-x}Mn_xSe$ superlattices. (T) denotes $T=77$ K.

Identification	MQW No. 37	MQW No. 43	MQW No. 58	MQW No. 103	MQW No. 105
Buffer	PbSe	PbSe	PbSe	$Pb_{1-x}Mn_xSe$	PbSe
d_{Buffer} (μm)	1.25	1.10	1.03	1.5	1.5
Number of periods	10	10	10	10	10
d_{PbSe} (nm)	46.5	19.2	13.0	25.0	25.0
$d_{Pb_{1-x}Mn_xSe}$ (nm)	46.5	19.2	13.0	25.0	25.0
x (from x ray)	0.0064	0.0134	0.0216	ca. 0.02	ca. 0.02
x (from E_g)		0.0077	0.012		
$N_{n,p}(T)$ (10^{17} cm^{-3})	+2.75	+4.40	+3.98	ca. −3	ca. −3
μ (T) (cm^2/Vs)	4559	3491	4200		

description of the properties of the molecular-beam-epitaxy (MBE)-grown PbSe/$Pb_{1-x}Mn_xSe$ samples is given and the experimental techniques are described. In Sec. III, the envelope function approximation (EFA) formalism for the band-structure calculation of semimagnetic IV–VI compound superlattices is presented. The energy eigenstates and wave functions in the Faraday as well as in the Voigt configuration are given and the consequences of the removal of the degeneracy of the eigenstates with respect to the position of the cyclotron center coordinate are discussed. In Sec. IV, experimental results of photoluminescence, interband magnetoabsorption, and optical four-wave mixing are compared with calculated interband transition and spin-flip transition energies. In particular, the consequences of the dispersion of the

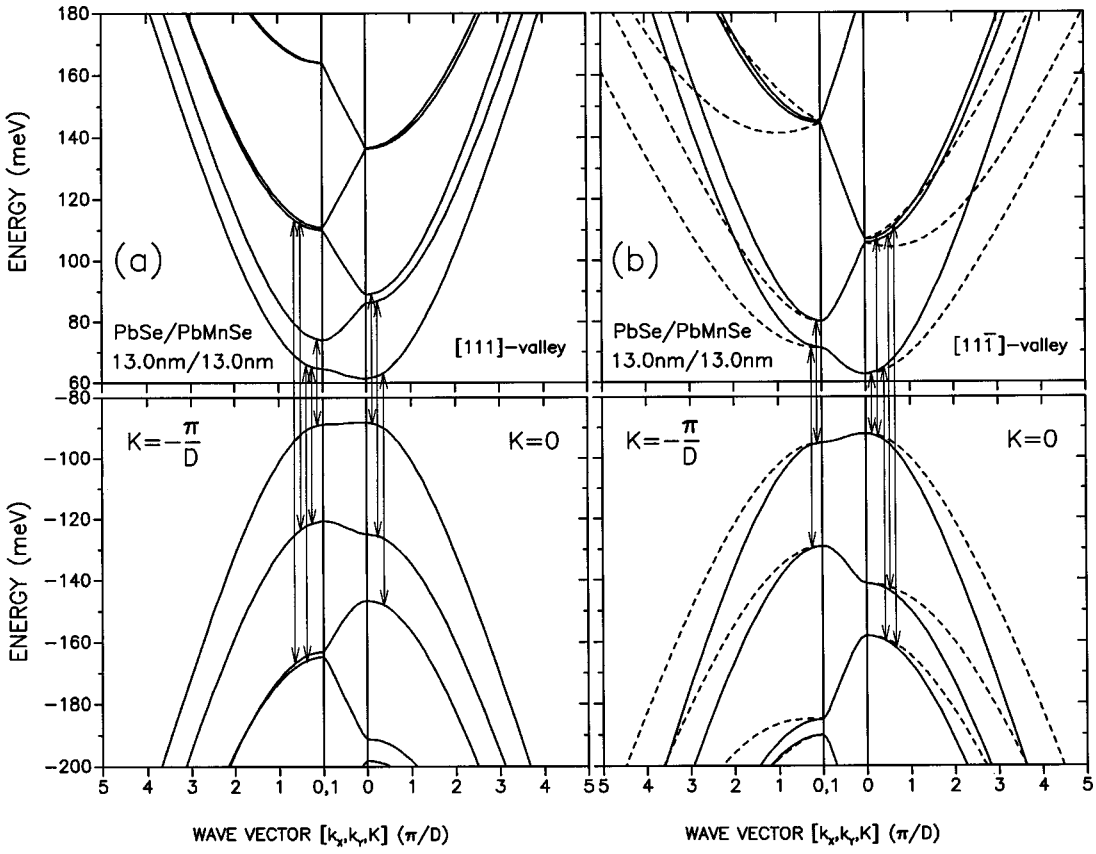

FIG. 1. $E(K,k_x,k_y)$ relationship as determined from EFA calculations for sample MQW No. 58 for the [111] valley (a) and the [$11\bar{1}$] valley (b). Abscissa in units of π/D, where D denotes the superlattice period. The dispersion along the superlattice growth direction between $K=0$ and $K=\pi/D$ is shown (central area of each figure part), as well as the dispersion as a function of $k_x\|$ [$1\bar{1}0$] (full lines) and $k_y\|$ [112] (dashed lines).

effective g factors due to the peculiarities of the superlattice band structure on the line shape of the observed CARS spectra is discussed.

II. EXPERIMENTAL DETAILS

A. MBE growth and sample parameters

The PbSe/$Pb_{1-x}Mn_xSe$ samples were grown by MBE as described by Frank *et al.*,[15] using PbSe, Se, and Mn effusion cells. A freshly cleaved (111) BaF_2 was used as a substrate onto which a comparatively thick PbSe layer was deposited prior to the growth of the superlattice in order to ensure nearly complete strain relaxation. The lattice mismatch between the PbSe layers and the $Pb_{1-x}Mn_xSe$ layers is comparatively small [a_{PbMnSe} (Å)$=6.127-0.00580\,x$ (Ref. 18)]. With such a small mismatch, the thicknesses of the $Pb_{1-x}Mn_xSe$ layers ($d<20$ nm) as well as that of the entire stack in the superlattices are well below the critical layer thickness. Thus the pseudomorphical $Pb_{1-x}Mn_xSe$ layers are under biaxial tensile strain with respect to the PbSe buffer and the PbSe layers in the superlattice. The structural parameters of the superlattices were determined by high-resolution x-ray diffraction using triple-axis diffractometry as described in Ref. 15, and are listed in Table I.

B. Interband magnetotransmission and photoluminescence

The measurement of magneto-optical interband transitions in PbSe/$Pb_{1-x}Mn_xSe$ superlattices ($x<0.02$) requires radiation wavelengths between 4.5 and 7.5 μm. Coherent radiation in this wavelength range was obtained using a liquid-nitrogen-cooled CO laser, which emits more than 100 laser lines that are approximately 4 cm^{-1} apart and are selected by a grating in the resonator. In addition, frequency doubling of a Q-switched CO_2 laser was employed by using a properly phase-matched Te crystal. The transmission spectra were recorded for a large number of different frequencies as a function of magnetic field up to 7T in Faraday configuration ($\mathbf{B}\|\mathbf{k}[111]$) with circularly polarized σ^+ and σ^- radiation and in Voigt configuration ($\mathbf{B}\perp\mathbf{k}$, $\mathbf{B}\|[110]$, $\mathbf{E}\|\mathbf{B}$). These experiments were performed in the temperature range of 1.7–20 K.

Since the hole concentration in the SL samples is about 5×10^{17} cm^{-3}, in magnetotransmission the lowest transitions are blocked because of the emptiness of the initial states (Landau levels) up to the Fermi energy. Photoluminescence in a magnetic field is used to study the low-energy region. For excitation of the photoluminescence a Q-switched Nd:YAG laser is used ($\lambda=1.06$ μm) (where YAG denotes yttrium aluminum garnet) and the luminescence radiation is observed with a photovoltaic HgCdTe detector.

C. Coherent anti-Stokes Raman scattering

CARS experiments were performed in order to get information on the spin splittings of the carriers in the PbSe/$Pb_{1-x}Mn_xSe$ superlattice structures. The spin resonance is a Raman-allowed transition in a semiconductor, and CARS is a particularly useful method of detecting these resonances. In narrow-gap semiconductors, the experiment has to be performed with infrared lasers in order to avoid too strong interband absorption.

In the CARS experiment, two laser beams (Q-switched CO_2 laser radiation) with frequencies ω_L and ω_S interact in the sample and generate radiation with new frequencies by nonlinear optical interactions. Among these, the frequency $\omega_{AS}=2\omega_L-\omega_S$ corresponds to the anti-Stokes frequency of a conventional Raman scattering experiment with pump laser ω_L and Raman shift $\omega_L-\omega_S$. The intensity I_{AS} at ω_{AS} is proportional to the square of a nonlinear susceptibility $\chi^{(3)}$, which is resonantly enhanced wherever $\omega_L-\omega_S$ corresponds to the transition energy of a Raman-allowed transition. In a magnetic field with orientation $\mathbf{B}\perp\mathbf{k}$, i.e., in Voigt geometry, the most important resonance of the nonlinear susceptibility is a spin-flip resonance if

$$\hbar(\omega_L-\omega_S)=g^*\mu_B B_{\mathrm{res}}, \tag{1}$$

where g^* is the effective g factor for the particular orientation of $\mathbf{B}$.

As outlined in Ref. 19, in these experiments complicated line shapes occur due to the interference of resonant and nonresonant parts of the nonlinear susceptibility. The nonlinear susceptibility has a nonresonant part χ^{NR} which is mainly real and resonances with real χ' and imaginary parts χ''. Thus the intensity is proportional to

$$|\chi|^2=|\chi^{\mathrm{NR}}|^2+|\chi'|^2+|\chi''|^2+2\chi^{\mathrm{NR}}\chi'. \tag{2}$$

The quantum-mechanical calculation of the resonant part of the susceptibility yields a sum over intermediate states $|b\rangle$, $|c\rangle$, and $|d\rangle$; in the sum, 24 terms like the one given in Eq. (3) (Ref. 20) have to be added:

$$\frac{\mu_{jkli}}{(\omega_{ba}-\omega_L-i\Gamma_{ba})(\omega_{ca}-(\omega_L-\omega_S)-i\Gamma_{ca})(\omega_{da}-\omega_{AS}-i\Gamma_{da})}. \tag{3}$$

μ_{jkli} stands for a product of four dipole matrix elements between consecutive intermediate states with field polarizations as indicated by the indices j, k, l, i; ω_{xy} represents the energy differences between levels of the scattering media; and Γ_{xy} indicates the level broadening of the states of the respective virtual transitions.

If in a CARS recording more than one transition is observed, then for each of them an expression like the one given in Eq. (3) has to be assumed. Real and imaginary parts are separated and added. Then the total line shape is fitted with $\chi^{(3)}_{\mathrm{NR}}$, the individual line positions, linewidths, and oscillator strengths being treated as adjustable parameters.

The setup used for the CARS experiments is similar to the one described in detail in Ref. 19. In multiple quantum wells

(MQW's) or superlattices (SL's), the susceptibility $\chi^{(3)}$ is strongly enhanced with respect to the corresponding bulk material due to the formation of minibands[21] and the resulting increase of the number of intermediate states. Despite the fact that I_{AS} is proportional to the square of the sample thickness (propagation of light perpendicular to the film surface) in superlattices, there are detectable signals with sample thicknesses well below 1 μm, whereas a homogeneous IV–VI compound film must have at least 5 μm thickness for CARS signals to be detectable.[14] In particular, this fact has the consequence that even in our samples with PbSe buffer layers of the order of 1 μm thickness, the entire CARS signal originates from the SL structure.

Because of the high peak powers (about 2 kW, 120 ns pulse duration) of the CO_2 lasers used for the experiments, minority carriers are photoexcited across the energy gap by two-photon absorption in *n*-type as well as in *p*-type samples, and the spin resonances of electrons and holes can be observed in one sample, regardless of their doping.

III. BAND MODEL

A. Envelope function formalism

Both PbSe and $Pb_{1-x}Mn_xSe$ ($x<0.03$) crystallize in the rock salt structure with a minimum direct gap at the *L* points of the Brillouin zone. The $\mathbf{k}\cdot\mathbf{p}$ treatment was initially given by Mitchell and Wallis,[22] taking into account the doubly degenerate valence and conduction bands and treating the two more distant conduction and valence bands in perturbation theory up to order k^2. A detailed presentation is also given in Refs. 9 and 23.

This treatment is readily extended to account for superlattice effects in the envelope-function approximation. This EFA formalism for the IV–VI compounds with the minimum direct gap at the *L* points of the Brillouin zone was described in detail by Kriechbaum[24,25] and will not be repeated here. In this treatment, the material parameters such as band-edge energies and the far-band contributions, as well as the interband matrix elements, are position dependent. Terms such as $k^2/m(z)$ have to be replaced by the hermitized term $k^2/m \rightarrow k(1/m)k$, $Pk \rightarrow (Pk+kP)/2$, in order to retain a Hamiltonian eigenvalue problem.

Results of such a SL band-structure calculation are shown in Fig. 1 for sample MQW No. 58. The energy-momentum relationship is shown in the central parts of the figures as a function of **K**, the SL Bloch vector in the range between 0 and π/D, where *D* denotes the SL period. Furthermore, the in-plane dispersion $E(k_x,k_y)$ is shown for $K=0$ and $K=\pi/D$ for both the longitudinal [111] and the oblique [111] valleys. The zero of energies for the valence and conduction bands is taken to be the center of the forbidden gap of PbSe. The calculation was performed for a normalized band offset $\Delta E_c/\Delta E_g=-0.4$. Due to inversion symmetry each state is doubly degenerate and there is mirror symmetry for $K\rightarrow -K$ for vanishing in-plane momentum. The arrows indicate the strongest dipole transitions. The dependence of the selection rules on *K* can be clearly seen.

Based on the subband energies and wave functions, the interband transition energies and their oscillator strengths were calculated numerically. For sample MQW No. 43, results for the lowest transitions are shown as a function of band offset in Fig. 2. The thickness of the calculated lines symbolizes the oscillator strength. In the region of staggered band alignment, the usual selection rules for the subband indices $\Delta n=0$ are violated. Experimental transition energies are indicated in the figure by horizontal lines.

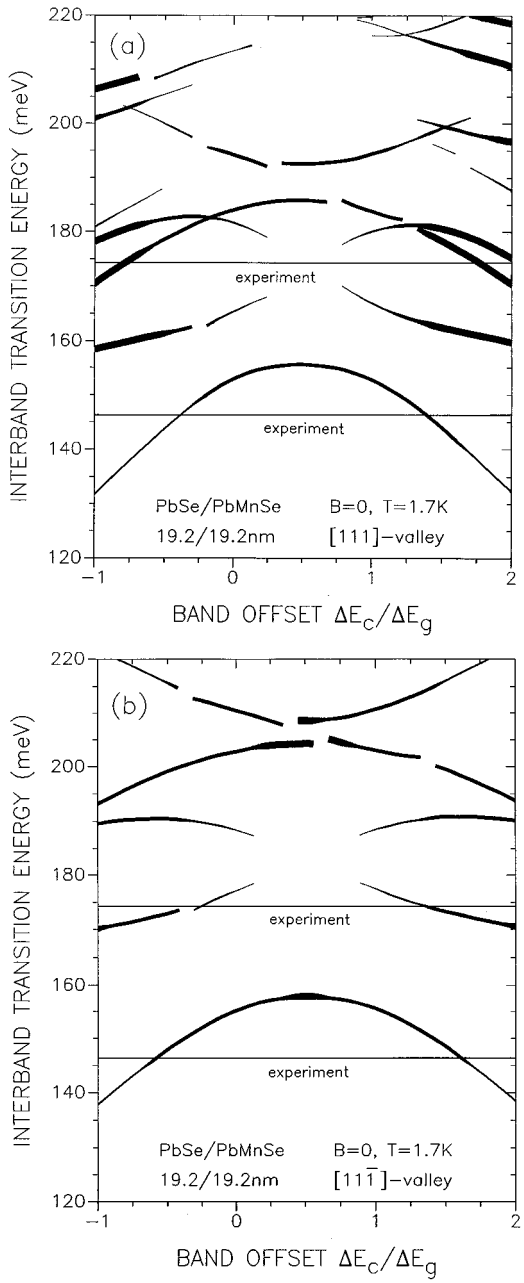

FIG. 2. Interband transition energies for the $PbSe/Pb_{1-x}Mn_xSe$ sample MQW No. 43 at $B=0$ vs band offset $\Delta E_c/\Delta E_g$ for both the [111] (a) and [111] (b) valleys. Note the change in selection rules. The oscillator strength is indicated by the width of the lines. The observed transition energies extrapolate for $B=0$ to energy gaps of 146.5 and 174.5 meV (see Fig. 11).

A magnetic field is included in this formalism by replacing the differential operator *k* by $k\rightarrow \nabla/i - e/c\mathbf{A}$, where $\mathbf{A}$ is the vector potential. The appropriate Hamiltonian for the *L* point is then given by

$$H=\begin{bmatrix} E_v-k_t^2/2m_t^+-k_3^2/2m_1^++g_t^+(\sigma_x\beta_1+\sigma_yB_2)+g_1^+\sigma_zB_3 & P_1\sigma_zk_3+P_t(\sigma_xk_1+\sigma_yk_2) \\ P_1\sigma_zk_3+P_t(\sigma_xk_1+\sigma_yk_2) & E_c+k_t^2/2m_t^-+k_3^2/2m_1^-+g_t^-(\sigma_xB_1+\sigma_yB_2)+g_1^-\sigma_zB_3 \end{bmatrix}. \tag{4}$$

Each of the entries is a (2×2) matrix. The m_t, m_1's and the g_t, g_1's are the far-band contributions to the masses and g factors, P_t and P_1 denote the two interband matrix elements, and σ_i are the Pauli spin matrizes. For Faraday geometry $\mathbf{B}\|\mathbf{k}$ this leads, for the oblique valleys, to a set of four coupled differential equations in two variables. For the longitudinal valley with its main axis parallel to the magnetic field and the growth direction, the electric and magnetic motion are completely decoupled. The resulting energy eigenstates are similar to Landau states superimposed on the electric subbands.

In Voigt geometry, with **B** parallel to the layers (i.e., along x direction), the vector potential **A** in the Landau gauge can be chosen to be parallel to the layers also (i.e., along the y direction) and the problem reduces to four coupled differential equations in one variable z (i.e., in the growth direction). The four envelope functions f_b ($b=1,\ldots,4$) are of the form

$$f_b=\exp(ik_Bx)\exp(ik_yy)Z_b(z-k_yl^2), \tag{5}$$

where the momentum k_B and the center coordinate $z_M=k_yl^2$ are good quantum numbers, although there is no decoupling of the electric and magnetic motion in Voigt geometry. The functions Z_b are obtained as solutions of the four coupled differential equations $Hf=Ef$, where the substitution

$$\begin{bmatrix} k_1 \\ k_2 \\ k_3 \end{bmatrix}=T\begin{bmatrix} k_B \\ k_y-z/l^2 \\ -i\partial/\partial z \end{bmatrix} \tag{6}$$

has been performed. T is the transformation matrix from the x,y,z coordinate system to the respective valley system and is given in Ref. 25. The degeneracy of the energy eigenstates with respect to the cyclotron center coordinate which is obtained for homogeneous bulk material is lifted in a superlattice. By this method the Landau-level energies and the allowed CARS transition energies are calculated for various band offsets.

B. Exchange interaction in $Pb_{1-x}Mn_xSe$

In the envelope-function approximation the exchange interaction between localized electrons and the valence band electrons[26,27] is determined by the symmetry group of the k vectors of the band edges. The spins of the electrons in the half filled d shell of the Mn^{2+} ions align according to Hunds rule to a total spin $S=\frac{5}{2}$. For the PbSe crystal structure (O_h) the symmetry group at the L point is D_{3d}. The minimum energy gap is formed by L_6^+ and L_6^- states. The Hamiltonian coupling these four states is given by symmetry to be

$$H=\begin{bmatrix} A^+S_3\sigma_z+a^+(S_1\sigma_x+S_2\sigma_y) & C(S\times k)_3\sigma_z+c[(S\times k)_1\sigma_x+(S\times k)_2\sigma_y] \\ C(S\times k)_3\sigma_z+c[(S\times k)_1\sigma_x+(S\times k)_2\sigma_y] & A^-S_3\sigma_z+a^-(S_1\sigma_x+S_2\sigma_y) \end{bmatrix}. \tag{7}$$

In a mean-field approximation, S is replaced by the thermal average $x\langle S\rangle$ over all orientations in the presence of a magnetic field B.

$$\begin{aligned} x\langle S\rangle &= x\ \mathrm{Tr}\ \rho(B)S/\mathrm{Tr}\ \rho(B) \\ &= x\{[(S+1)/2]\coth([(S+1)/2]\beta g\mu_BB) \\ &\quad -\coth(\beta g\mu_BB/2)\}, \end{aligned} \tag{8}$$

where x is the volume concentration of the Mn^{2+} ions. Interaction effects of the magnetic moments of the d electrons located at different sites are included by allowing S to be a variation parameter S_0, and $\beta=1/k_BT$ is replaced by $1/k_B(T+T_0)$.[28] By fitting temperature-dependent magnetization data of bulk $Pb_{1-x}Mn_xSe$, the parameters S_0 and T_0 are obtained.[7] The six exchange parameters A^+, A^-, a^+, a^-, C, and c are obtained by fitting the interband fan charts and CARS data of bulk $Pb_{1-x}Mn_xSe$.[8,10] It turned out that the interband exchange parameters C and c are negligible. That supports the assumption of a pointlike exchange interaction between the valence electrons and the localized d electrons at **R**:

$$H_{\mathrm{exch}}=J\delta(\mathbf{r}-\mathbf{R})\mathbf{S}\cdot\boldsymbol{\sigma}. \tag{9}$$

C. Band-structure calculation in semimagnetic superlattices

The exchange interaction between the magnetic ions and the mobile carriers is restricted to the $Pb_{1-x}Mn_xSe$ layers, the material that happens to be, in this case, the larger band-gap material. For the calculations of the eigenstates and eigenfunctions, the two contributions to the total Hamiltonian [Eqs. (4) and (7)] have to be combined and the corresponding differential equation system is solved numerically.

Calculations were made for several band offsets. From the temperature and magnetic-field dependence of the CARS data we had determined that in the SL's with Mn contents lower than 2%, the electron wave functions are concentrated in the $Pb_{1-x}Mn_xSe$ layers, whereas the hole wave functions

TABLE II. Band and exchange parameters of the PbSe/$Pb_{1-x}Mn_xSe$ superlattices for $T=1.7$ K. The far band parameters are taken from published data for PbSe (Refs. 10 and 19).

	PbSe layer (Ref. 19)	$Pb_{1-x}Mn_xSe$ layer in MQW No. 43 (Ref. 10)	$Pb_{1-x}Mn_xSe$-layer in MQW No. 58 (Ref. 10)
E_g (meV)	146.3	175.9	192.0
x		0.0077	0.012
$2P_\perp^2/m_0$ (eV)	3.60	3.60	3.55
$P_\perp/P_\parallel$	1.35	1.35	1.4
A (meV)		−204	−204
a_1 (meV)		−215	−215
B (meV)		7	7
b_1 (meV)		91	91
T_0 (K)		0.4	1.0
S_0		2.35	2.15

are concentrated in the PbSe layers. Thus the offset corresponds to a staggered superlattice system. Also, interband transmission experiments on a set of PbSe/$Pb_{1-x}Mn_xSe$ superlattices have confirmed this band alignment (cf. Fig. 2).[16]

In the following, calculated data are shown for an offset $\Delta E_c/\Delta E_g=-0.4$, i.e., the conduction-band edge of the $Pb_{1-x}Mn_xSe$ layers is below that of the PbSe layers. For the SL samples listed in Table I, the eigenstates were calculated as a function of magnetic field for the Faraday geometry using the band and exchange parameters of Table II. An example is shown in Fig. 3 for sample MQW No. 43 for the [111] valley and $K=0$. In the magnetic-field and temperature range where the magnetization varies strongly with temperature, the interband transitions for σ^+ and σ^- transitions are quite different from each other. The selection rules are indicated in the fan charts. Since for PbSe/$Pb_{1-x}Mn_xSe$ the interband transitions are indirect in real space, the selection rules do not entirely follow the usual ones, i.e., $\Delta n=0$ for the electric subbands involved in the interband transitions, and bulklike selection rules for the Landau states, as expected for a type-I superlattice.

For the Voigt configuration, in Fig. 4 energy eigenstates of sample MQW No. 43 are shown versus magnetic field. In this configuration, the center coordinate z_M of the cyclotron orbits is still a good quantum number, which is conserved in dipole transitions. Strong dipole transitions for linear polarization **E**||**B** are indicated. In contrast to bulk material, the energy degeneracy is lifted in the SL's. This calculation was performed for sample MQW No. 43 with the center coordinate z_M in the middle of the PbSe layers [Fig. 4(a)] and for z_M in the middle of the $Pb_{1-x}Mn_xSe$ layers [Fig. 4(b)]. The heavy bars along the ordinate axis indicate the width of the energy dispersion with respect to the superlattice Bloch wave number K. The Voigt configuration poses an interesting example for competing confinement effects, viz. the electrical confinement due to the superlattice potential and the parabolic magnetic potential. This is clearly reflected in the crossing behavior of the Landau levels as shown in Fig. 4. Furthermore, the increasing magnetic confinement draws the wave function into the well, which is reflected in the decrease of the lowest eigenstate energies with respect to the

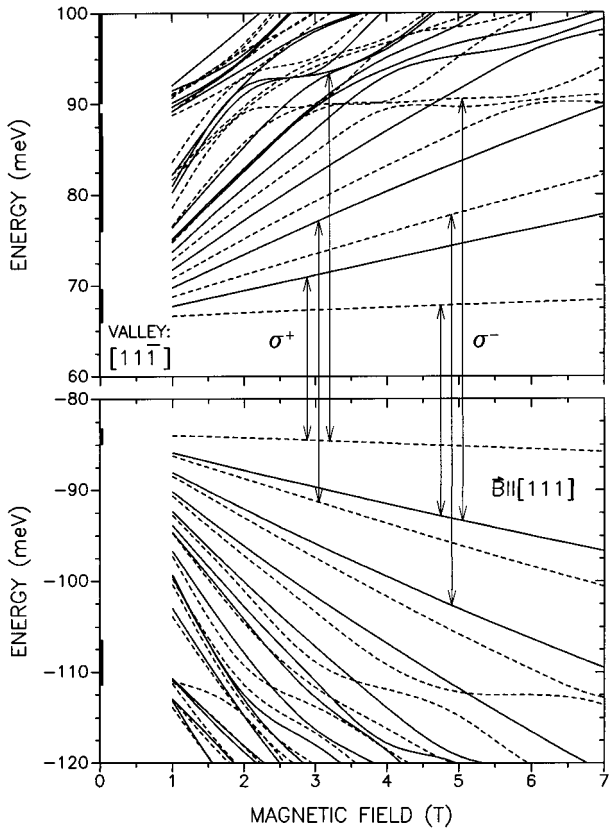

FIG. 3. Conduction- and valence-band Landau levels in the Faraday configuration of PbSe/$Pb_{1-x}Mn_xSe$ sample MQW No. 43 (19.2 nm/19.2 nm; $x=0.0077$) as a function of magnetic field parallel to the [111] growth direction for a [$\bar{1}\bar{1}\bar{1}$] valley and a normalized band offset $\Delta E_c/\Delta E_g=-0.4$ at $T=1.7$ K. Full and dashed lines for the $s=+\frac{1}{2}$ and $s=-\frac{1}{2}$ Kramers pair, respectively ($K=0$); arrows indicate strongest allowed transitions.

corresponding band-edge energy (with increasing magnetic field), and which is clearly seen for the lowest hole states.

However, the spin splitting has an additional dependence on z_M in the diluted magnetic superlattices, due to the spatial modulation of the Mn^{2+} ion density and thus the corresponding modulation of the exchange interaction. Consequently, the spin-flip transition energies, i.e., the g factors, depend on z_M in both the conduction and valence bands. As for these superlattices, the electrons are predominantly located in the $Pb_{1-x}Mn_xSe$ layers; the Landau states are shown as well for center coordinates in the $Pb_{1-x}Mn_xSe$ layers.

Figure 5 shows the dependence of the superlattice eigenstates in Voigt geometry for a constant applied field as a function of the center coordinate for the sample MQW No. 58 and a normalized conduction-band offset $\Delta E_c/\Delta E_g=-0.4$ for the longitudinal and one oblique valley. It should be noted that for certain regions of z_M the sequence of the levels does not necessarily correspond to that found in bulk material and, in particular, level crossings occur at certain values of z_M. In Fig. 6, the square of the wave functions for electron and hole states ($|\Psi|^2$ for spin-up and spin-down states do not differ remarkably) are plotted together with the conduction- and valence-band edges for the sample MQW No. 58. For the left panels the position of the center coordinate is chosen to be in the middle of the PbSe layers. For the

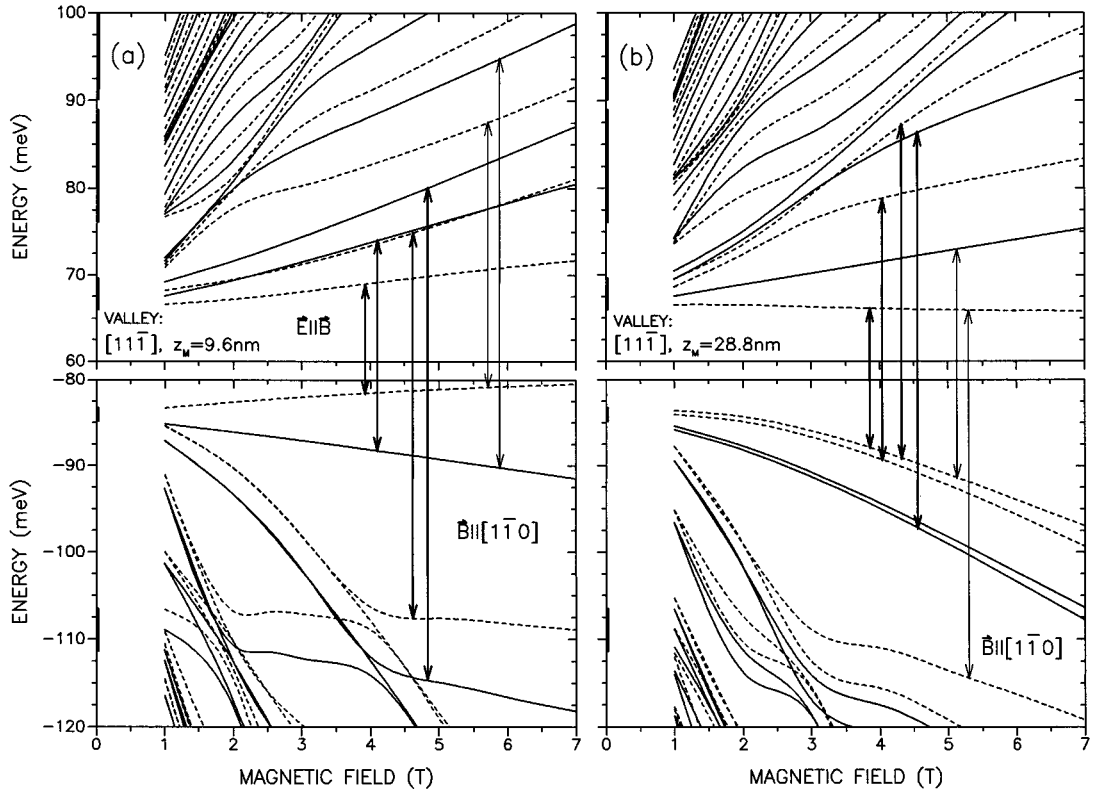

FIG. 4. Landau levels in the Voigt configuration of PbSe/$Pb_{1-x}Mn_xSe$ sample MQW No. 43 (19.2 nm/19.2 nm; $x=0.0077$) for the conduction and valence bands for an in-plane magnetic field, parallel to the [110] direction, for the [111] valley and a normalized band offset $\Delta E_c/\Delta E_g=-0.4$ at $T=1.7$ K. Full and dashed lines for $s=+\frac{1}{2}$ and $s=-\frac{1}{2}$, respectively; arrows indicate strongest allowed transitions (fine arrows for a smaller oscillator strength).

electrons, the wave function is extended over several layers, whereas the hole wave function is localized in the PbSe layers. Although the center coordinate z_M for the electrons is in the middle of the PbSe layers, the maxima of the square of the electron wave functions are in the adjacent $Pb_{1-x}Mn_xSe$ layers. For the right panels, the center coordinate is chosen to be in the middle of the $Pb_{1-x}Mn_xSe$ layers. Especially in the panels with z_M in the barrier, the competing confinement effects of magnetic field and superlattice can be seen.

Furthermore, in Fig. 7 the dependence of the g factor of electrons and holes is shown as a function of the position of the center coordinate. The spin-flip transition energies depend on z_M for both the electrons and the holes. These data are shown for the [111] valley ($\Phi=35.26°$), the [111] and [111] valley, both $\Phi=90°$.

IV. RESULTS AND DISCUSSION

A. Photoluminescence

Figure 8 shows a comparison of photoluminescence (PL) spectra taken at $B=0$ and 6.9 T, respectively, for a PbSe epitaxial film (a) and the superlattice MQW No. 58 (b). The SL luminescence is shifted to higher energies compared to bulk material. In a magnetic field, the SL emission is split into two lines [see also insert of Fig. 8(b)]. We never observed such a splitting in a homogeneous IV-VI semiconductor. These observations show that in the SL there is an interband transition that is energetically close to the PbSe gap. In a type-I SL with effective masses like PbSe and a well width of 13 nm, the transition between the lowest subbands would be shifted considerably to higher energies. As can be seen from Fig. 2, this is not true for a staggered band alignment as in our case.

Exact transition energies should be taken from interband transmission experiments, since the PL frequencies are shifted due to many-body effects.[29] In this context we want to emphasize that the data shown in Figs. 8(a) and 8(b) are taken at identical excitation conditions.

B. Interband magnetoabsorption

It is well known that interband magnetoabsorption can give valuable information on the electronic band structure of quantum-well and superlattice systems. In our case, due to the rather large dielectric constants, excitonic effects are negligible and thus the observed transition energies can be even directly compared with the EFA calculations. However, in our experimental data, which are shown below, the magnetotransmission spectra are influenced by bulklike interband transitions that take place in the energy range investigated not only in the PbSe/$Pb_{1-x}Mn_xSe$ layers but in the underlying PbSe buffer layer as well. For PbSe/$Pb_{1-x}Mn_xSe$ superlattice samples this phenomenon cannot be avoided, since in order to improve their structural quality, they had to be grown on comparatively thick PbSe buffers ($d\approx\mu$m) and not directly on the (111) BaF_2 substrates. Consequently, in order to be able to distinguish between the transitions originating from the buffer and from the PbSe/$Pb_{1-x}Mn_xSe$ layers in our

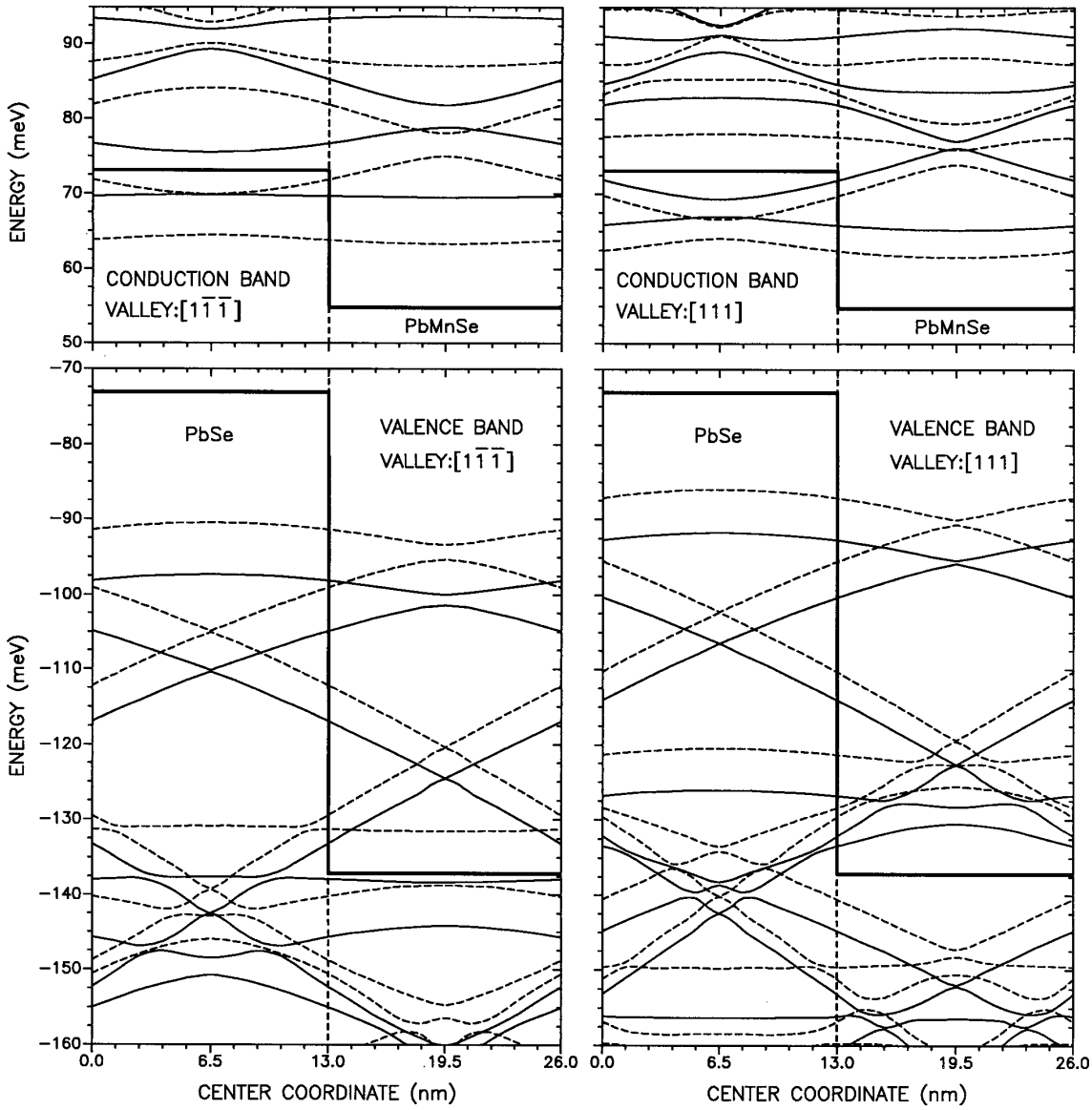

FIG. 5. Energy levels of sample MQW No. 58 vs the center coordinate for an applied in-plane magnetic field ($B=3.5$ T, parallel to the [110] direction). Left-hand panels, [11 1] valleys; right-hand panels, [111] valley. Full and dashed lines for $s=+\frac{1}{2}$ and $s=-\frac{1}{2}$. Bold lines indicate the band edges at $B=0$.

SL samples, we first measured interband magnetoabsorption in homogenous epilayers of PbSe and $Pb_{1-x}Mn_xSe$.

In homogeneous PbSe, the g factors of valence and conduction bands are almost identical. Consequently, σ^+ and σ^- polarized interband transitions occur at the same magnetic field [see Fig. 9(a)]. The trace shown there is taken in Faraday geometry with linearly polarized light. If there were a σ^+/σ^- splitting, then each transmission minimum should occur twice). Due to the difference of the exchange interaction in valence and conduction bands,[10] the degeneracy of σ^+ and σ^- transitions is lifted in $Pb_{1-x}Mn_xSe$ [see Fig. 9(b)].

In the superlattice samples, in principle two different kinds of transitions are observed. One of them exhibits a very small σ^+ and σ^- splitting, whereas the other one shows a considerably larger one, but smaller than in homogeneous $Pb_{1-x}Mn_xSe$ with comparable Mn content, indicating a more complex scheme of the magneto-optical transitions [see Fig. 10(a)]. Figure 10(b) demonstrates that the splitting tends to zero with increasing temperature.

Fan charts of these transitions are shown in Fig. 11. Due to the high hole concentration ($p\approx 4\times 10^{17}$ cm^{-1}) corresponding to a Fermi energy of about 20 meV, the transitions involving the lowest electric subbands in the valence band are blocked at smaller magnetic fields. The calculated transition energies are shown as well for the [111] [Fig. 11(a)] and the oblique [111] valleys [Fig. 11(b)]. It turns out that the σ^+ and σ^- splitting is much more pronounced for the oblique valleys, both experimentally and theoretically. The broken and dotted lines correspond to the calculated strongest interband transitions with the selection rules as shown in Fig. 4. The agreement between experimental and calculated data is very good, particularly having in mind that the band and exchange parameters are taken from bulk PbSe and $Pb_{1-x}Mn_xSe$ materials and layer widths from the x-ray dif-

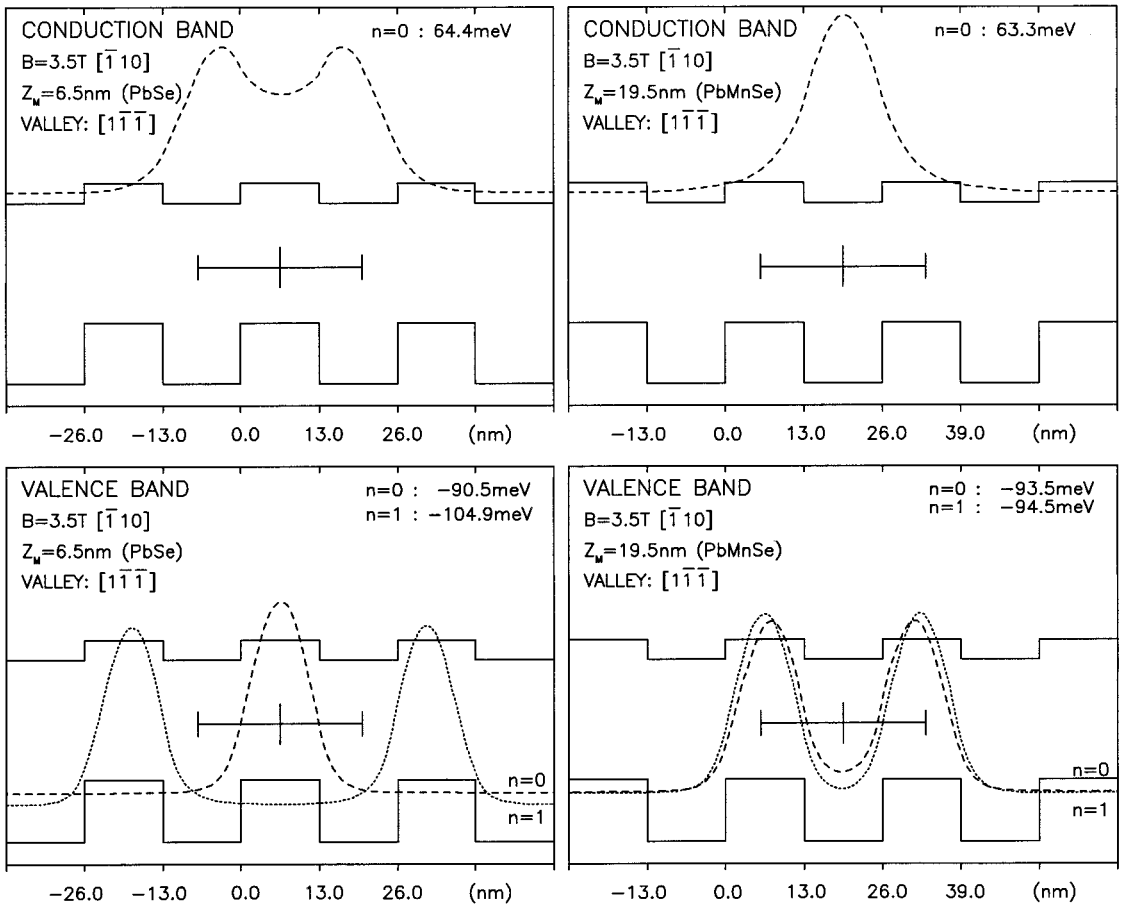

FIG. 6. Schematic diagram of band edges vs z coordinate (growth direction). Dashed curves: square of the wave functions of the 0^- levels of the conduction and valence bands for z_M in the center of the PbSe layers (6.5 nm) (left-hand panels). Dotted curves: 1^- levels of the valence band. Whereas the hole wave function is essentially confined in the PbSe layers, the electron wave function exhibits extrema in the $Pb_{1-x}Mn_xSe$ layers but appreciable probability in the PbSe layers as well. Right-hand panels for z_M=19.5 nm, corresponding to the center of the $Pb_{1-x}Mn_xSe$ layers. (The wave functions of the corresponding 0^+,1^+ levels are not shown because of their nearly identical structure.)

fraction, and thus no adjustable parameters enter into the calculations apart from the band offset, which was taken to be $\Delta E_c/\Delta E_g=-0.4$.

Since the data are taken in transmission, the influence of the rather thick PbSe buffer must be considered, particularly for the series of transitions that do not exhibit a $\sigma^+-\sigma^-$ splitting [Fig. 11(a)]. For the PbSe buffer the magnetotransmission is much more influenced by the transitions in the three oblique valleys than due to the transitions involving the Landau levels of the [111] valley. In this Figure calculated fan charts are plotted for the respective SL transitions for $\Phi=0°$ and the PbSe transitions for $\Phi=70.53°$. Unfortunately, due to the finite level width, the transitions from the SL and from the PbSe buffer are not resolved and the experimental points are, rather, located in between of them. However, for the transitions involving the oblique valleys of the SL, we observe signatures that are ambiguously attributed to the particular band structure of the $PbSe/Pb_{1-x}Mn_xSe$ layers.

The open circles in Fig. 11(b) indicate another type of transition originating from the superlattice. Extrapolation to $B=0$ yields an energy of about 165 meV, which corresponds to a transition at $K=\pi/D$ from the second electric subband in the valence band to the first one in the conduction band. In contrast to other transitions within the $[11\bar{1}]$ valleys, there is no $\sigma^+-\sigma^-$ splitting occurring. For σ^+ polarization there are two transitions (indicated as 1 and 2 in Fig. 11) that are close together and not resolved experimentally. The transmission minimum is observed in between. For σ^-, the transition indicated as 3 in Fig. 11 has energies in between the two σ^+ transitions and is observed at the same position as the superposition of the two lines with σ^+ polarization. The different slope of the transition energy versus magnetic field results from the different in-plane curvatures $E(k_x,k_y)$ at $K=0$ and $K=\pi/D$, respectively. Despite the difficulties due to level broadening and the modulated magnetotransmission due to the buffer as well as due to the rather large value of E_F, the transitions within the oblique valley of the $PbSe/Pb_{1-x}Mn_xSe$ structure yield clear evidence of the superlattice band structure, in particular through transitions involving levels associated both the $K=0$ and the $K=\pi/D$ states.

C. Optical four-wave mixing

Coherent anti-Stokes Raman scattering experiments were performed on the superlattice samples listed in Table I at

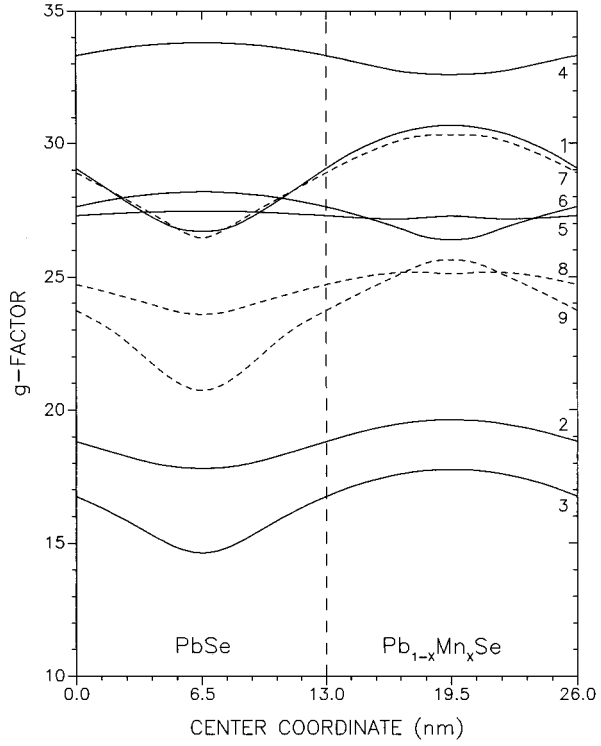

FIG. 7. g factor vs center coordinate z_M for sample MQW No. 58 for an applied in-plane magnetic field of $B=3.5$ T for B parallel to the [110] direction at $T=1.7$ K, for three valleys. Full lines ($n=0$): 1, CB [11 1] valley; 2, CB [111] valley; 3, CB [111] valley; 4, VB [11 1] valley; 5, VB [111] valley; 6, VB [111] valley. Dashed lines ($n=1$): 7, VB [11 1] valley; 8, VB [111] valley; 9, VB [111] valley.

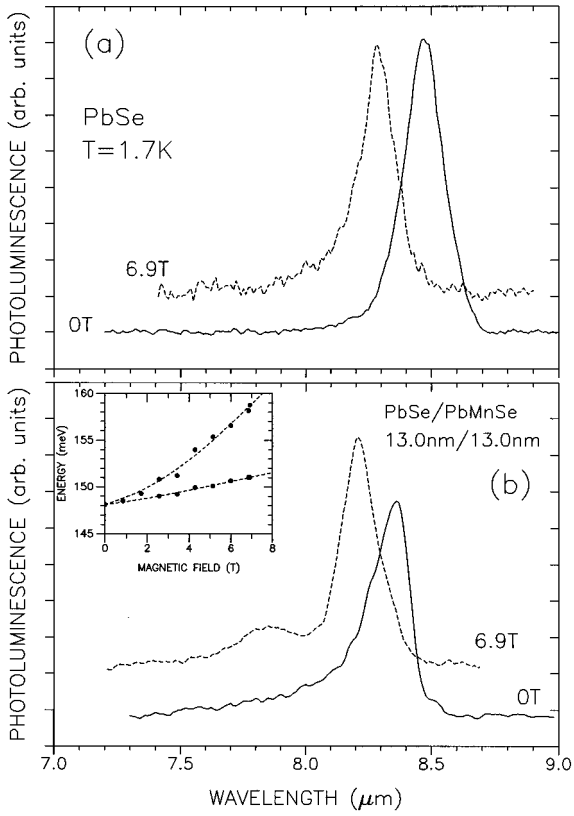

FIG. 8. Photoluminescence of a PbSe epilayer (a) and the PbSe/$Pb_{1-x}Mn_xSe$ sample MQW No. 58 (b) for $B=0$ and $B=6.9$ T in the Faraday configuration with $\mathbf{B}\|[111]$. Inset: peak luminescence as a function of the magnetic field.

temperatures between 1.7 and 20 K. Experimental recordings were made by sweeping the magnetic field, keeping the frequency difference $\omega_L-\omega_S$ fixed. Figure 12(a) shows a typical recording for the superlattice MQW No. 58. There are four transitions resolved, corresponding to electrons and holes in the $\Phi=90°$ and in the $\Phi=35°$ valleys, respectively.

A line-shape analysis as described in Sec. II C has been performed and the result is also plotted in Fig. 12(a). Figure 12(b) shows the imaginary parts for the four transitions, Fig. 12(c) the real parts. Line positions correspond to the maxima in Fig. 12(b). A particular property of the superlattice is the high nonresonant contribution to $\chi^{(3)}$ [see broken horizontal line in Fig. 12(c)], which is comparable to the amplitude of the strongest transition. In homogeneous $Pb_{1-x}Mn_xSe$ [see Fig. 12(d)] the nonresonant contribution is much weaker. A direct experimental signature for the large nonresonant contribution is the high signal for magnetic fields above the last resonance [see Fig. 12(a)], an experimental result which is only observed in superlattices. Whenever resonance positions are specified in the following, they were determined by this procedure.

In order to identify in which layers the electrons or holes are confined, the temperature and magnetic-field dependence of the resonance positions was measured. In Fig. 13 experimental recordings at various temperatures are shown. Apparently, there is only a minute temperature dependence of hole and of electron resonance positions, in contrast to equivalent data taken for bulk $Pb_{1-x}Mn_xSe$ samples with comparable Mn content.[10] There the two-hole resonances exhibit a considerable shift of the resonant magnetic fields to higher values with increasing temperature, whereas the electron resonances shift more weakly, but to lower field values. For the PbSe/$Pb_{1-x}Mn_xSe$ superlattices, only the highest resonance position, the one corresponding to the electrons, shifts with increasing temperature a little bit to lower resonant magnetic fields. The magnetic-field dependence of effective g factors obtained for two SL samples is compared to bulk PbSe and $Pb_{1-x}Mn_xSe$ data, respectively, in Fig. 14. It is seen that almost no typical semimagnetic behavior is observed in the SL's, in strong contrast to the bulklike $Pb_{1-x}Mn_xSe$ epilayer sample. On the other hand, the comparison clearly shows that the CARS signals can not originate from the PbSe buffer layers.

Both the weak temperature and the magnetic-field dependence of the g factors demonstrate that the holes cannot be confined in the $Pb_{1-x}Mn_xSe$ layers. On the contrary, even not only in the lowest subbands they are essentially localized in comparatively deep PbSe wells. For the electrons, where the exchange interaction is weaker, such a strict exclusion cannot be deduced from these qualitative arguments.

In Fig. 15 the calculated magnetic-field dependence of the effective g factors is shown for the offset $\Delta E_c/\Delta E_g=-0.4$, the value used for all the calculations in Sec. III. The center coordinates are taken in the middle of the respective layers and $k_B=0$. Comparison of Figs. 15(a) and 15(b) with 14(c) and 14(d) shows that in the experiment there is a weaker

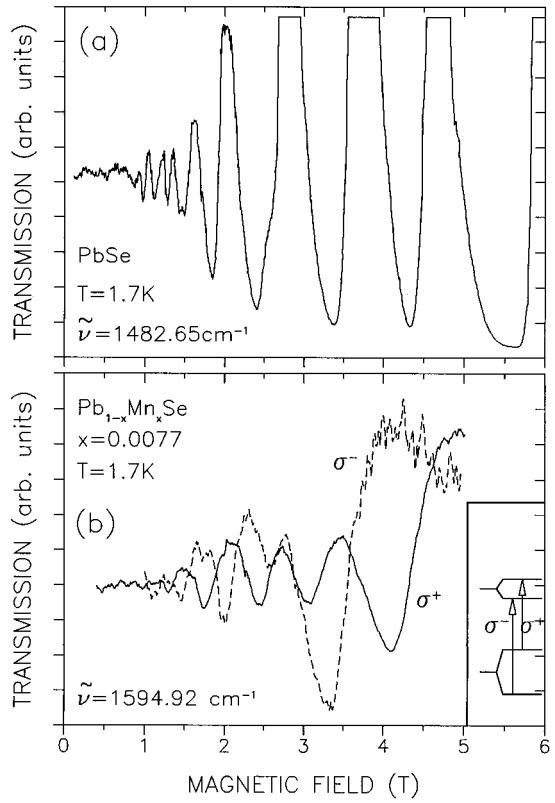

FIG. 9. Magnetotransmission in the Faraday configuration for a PbSe epilayer (a) and a $Pb_{1-x}Mn_xSe$ epilayer with $x=0.0077$ (b) at $T=1.7$ K.

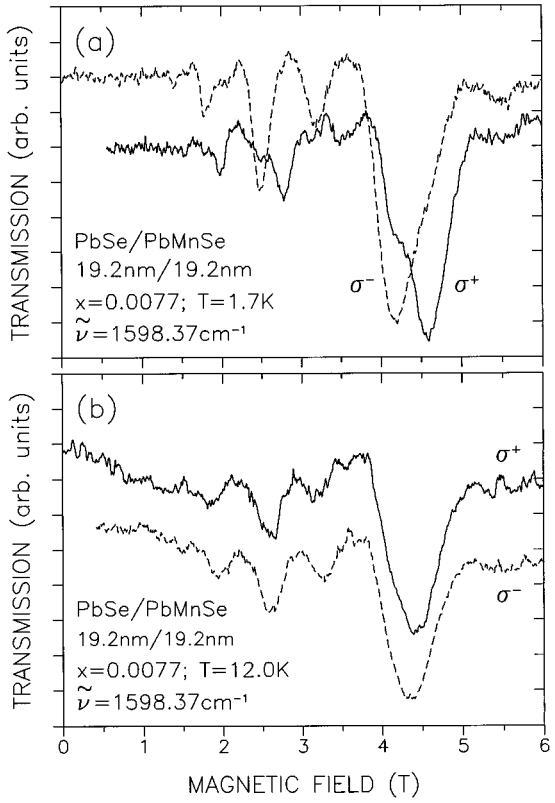

FIG. 10. Magnetotransmission in the Faraday configuration for $PbSe/Pb_{1-x}Mn_xSe$ sample MQW No. 43 at $T=1.7$ K (a) and at $T=12$ K (b).

magnetic-field dependence of the g factors than expected theoretically. In the captions to Figs. 14 and 15, all transitions are identified. To see the correspondence between both figures one must keep in mind that transitions that are too close together, such as 5 and 6 in Fig. 15, are not resolved experimentally. For the valence-band transitions a, b, and c (Fig. 15) due to the high hole density and the averaging discussed below in Fig. 16, only one [transition 2 in Fig. 14(c)] (respectively two peaks [transitions 2, 3 in Fig. 14(d)]) are observed experimentally. Consequently, 1 in Fig. 14(c) has to be compared to 4 in Fig. 15(a), 3 in Fig 14(c) is due to the nonresolved superposition of 5 and 6 in Fig. 15(a). The transition labeled 2 in Fig. 14(c) is to be compared to a nonresolved superposition of c and b. Transition a in Fig. 15(a) is due to a valley with $\Phi=35°$ which experimentally in general has a poorer intensity than the valleys with $\Phi=90°$ and is not seen in this sample. But, as mentioned above, the identification of the valence-band transitions is more diffi-

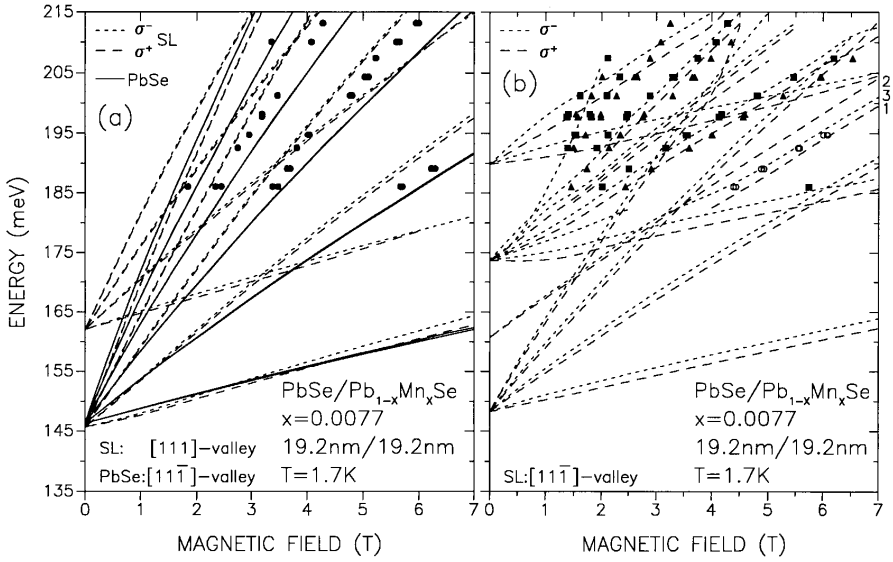

FIG. 11. Experimental and calculated fan charts of interband transition energies vs. magnetic field in Faraday configuration with $\mathbf{B}\|[111]$ for the [111] and oblique [111] valleys. ○, ●: transitions which coincide for σ^+ and σ^- polarization; ■: σ^- polarization; ▲: σ^+ polarization; lines: calculated.

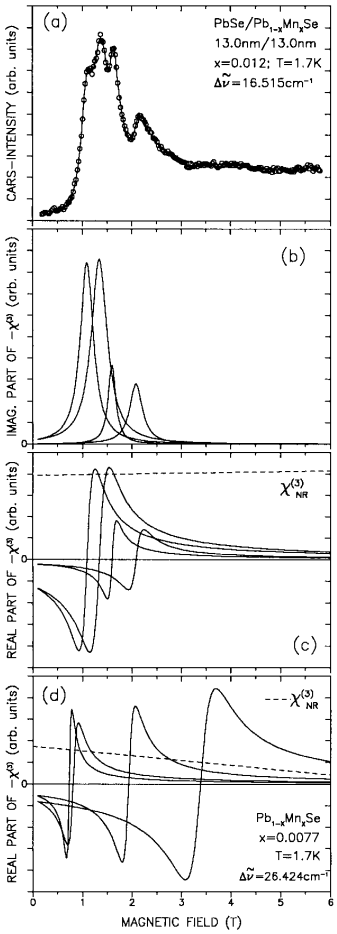

FIG. 12. (a) Experimental CARS data for $PbSe/Pb_{1-x}Mn_xSe$ sample MQW No. 58 at $T=1.7$ K and calculated data (full line). The latter were determined by a superposition of real and imaginary parts of $\chi^{(3)}$ according to (b) and (c). (b) Imaginary part of $\chi^{(3)}$ (4 spin resonances observed). (c) Real part of $\chi^{(3)}$ for the four resonances. Dashed line: nonresonant background to $\chi^{(3)}$. (d) Same as (c) but for a $Pb_{1-x}Mn_xSe$ epilayer sample with a comparable Mn content of $x=0.0077$. [For g factors as a function of the magnetic field, see Fig. 14(b)]. Note the smaller nonresonant background to $\chi^{(3)}$ in the spatially homogeneous layer especially for higher magnetic field.

cult. The correspondence between Figs. 14(d) and 15(b) is accordingly, despite the fact that in the superlattice with the shorter period two valence-band transitions [2 and 3 in Fig. 14(d)] can be resolved.

We assume that the slight magnetic-field dependence of g factors, which should remain even for electrons confined in $Pb_{1-x}Mn_xSe$ and holes in PbSe, is reduced in experiment by averaging center coordinates and wave vectors due to the relatively high carrier densities of our samples, particularly at small magnetic fields. Figure 16 shows a calculated CARS line shape in comparison with the experimental result. For the calculation, the spin flip in the $n=0$ conduction-band and the $n=1$ valence-band level is assumed (the sample is p doped). Contributions to the CARS intensity originating from all center coordinates and k_B values up to $\hbar^2 k_B^2/2m^*=g^*(k_B=0)\mu_B B$ are integrated. This k_B limit is rather arbitrary; however, the dependence of g^* on k_B is not very strong in this range.

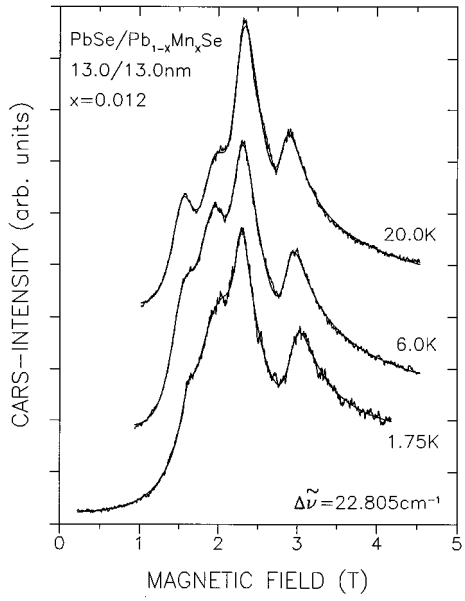

FIG. 13. CARS intensity as a function of the magnetic field for sample MQW No. 58 at $T=1.7$, 6, and 20 K.

An agreement, e.g. as seen in Fig. 16 at intermediate and high magnetic fields, encourages us to perform an identification of the observed transitions and a determination of the band offset by a comparison of experimentally observed g factors with theoretical calculations (see Fig. 17 for MQW No. 58 and Fig. 18 for MQW No. 43). The lines represent the calculated dependence of the spin splittings of the $n=0$ Landau levels in the different valleys of the conduction band and of the $n=1$ levels of the valence band. For the valence band, we present the $n=1$ levels, since the samples are p doped. The Fermi level cannot be obtained from magnetoconductivity and Hall measurements because there is a 1-μm-thick PbSe buffer layer that prevents the determination of a precise carrier concentration in the SL's, which have a total thickness of 0.26 and 0.38 μm, respectively. From the blocking of interband transitions in magnetotransmission, we estimate the Fermi energies to be about 20 meV. Due to the problems mentioned above with the discrepancy of calculated g factors at $k=0$ with the experiments, we used a relatively high magnetic field for this comparison.

The full curves in Figs. 17 and 18 represent spin-flip transitions between levels with a center coordinate in $Pb_{1-x}Mn_xSe$, broken curves correspond to levels with a center coordinate in PbSe. A distinctive qualitative feature is the strong increase of g factors of holes at those band offsets where the confinement changes from PbSe to $Pb_{1-x}Mn_xSe$ layers. Since the exchange interaction for holes is much stronger than for electrons, the corresponding changes for the electrons with varying band offset turn out to be much smaller. For a quantitative understanding of these dependences, the probability distribution of electron and hole states is required (see Fig. 6).

For all samples, a simultaneous crossing of calculated lines and experimental data occurs for all transitions for a band offset $\Delta E_c/\Delta E_g=-0.4$. In particular, the lowest g factor cannot be obtained for another band alignment.

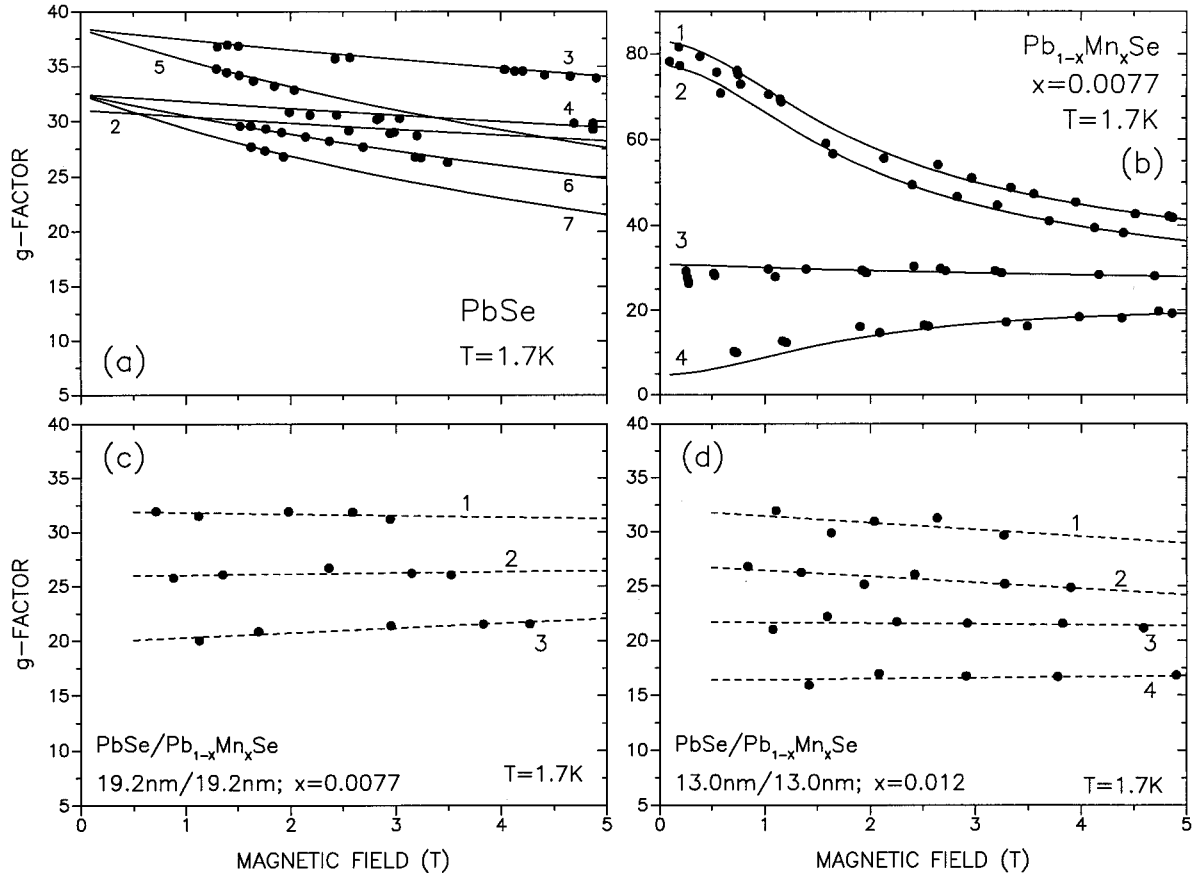

FIG. 14. Magnetic-field dependence of the effective g factors. (a) Homogeneous PbSe; (b) $Pb_{1-x}Mn_xSe$; (c) MQW No. 43; (d) MQW No. 58. ●, measured by CARS; full lines, calculated with the band and exchange parameters as listed in Table II; dashed lines, guide for the eye. The transitions are identified as (a) 1, VB [11 1] valley, $n=0$; 2, VB [111] and [111] valleys, $n=0$; 3, CB [11 1] valley, $n=0$; 4, CB [111] and [111] valleys, $n=0$; 5, CB [11 1] valley, $n=1$; 6, CB [111] and [111] valleys, $n=1$; 7, CB [111] and [111] valleys, $n=2$. (b) 1, VB [11 1] valley; 2, VB [111] and [111] valleys; 3, CB [11 1] valley; 4, CB [11] and [111] valleys. (c) 1, CB [11 1] valley; $n=0$; $z_M=28.8$ nm ($Pb_{1-x}Mn_xSe$) and VB [11 1] valley; $n=1$; $z_M=9.6$ nm (PbSe); 2, VB [111] and [111] valleys; $n=1$; $z_M=9.6$ nm (PbSe); 3, CB [111] valley; $n=0$; $z_M=28.8$ nm ($Pb_{1-x}Mn_xSe$). (d) 1, CB [11 1] valley; $n=0$; $z_M=19.5$ nm ($Pb_{1-x}Mn_xSe$); 2, VB [11 1] valley; $n=1$; $z_M=6.5$ nm (PbSe); 3, VB [111] valley; $n=1$; $z_M=6.5$ nm (PbSe); 4, CB [111] valley; $n=0$; $z_M=19.5$ nm ($Pb_{1-x}Mn_xSe$). ([11 1]≙Φ=35°; [111]≙Φ=90°; [111]≙Φ=90.0°).

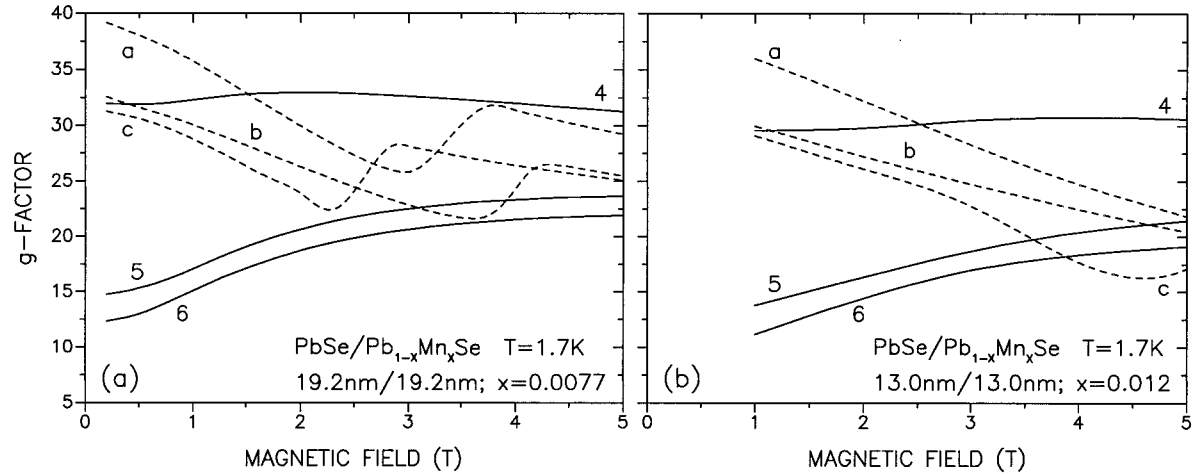

FIG. 15. Calculated magnetic-field dependence of the effective g factors of the sample MQW No. 43 (a) and MQW No. 58 (b). The transitions are identified as a, VB [11 1] valley, $n=1$, z_M in the center of the PbSe layer; b, VB [111] valley, $n=1$, z_M in the center of the PbSe layer; c, VB [111] valley, $n=1$, z_M in the center of the PbSe layer; 4, CB [11 1] valley, $n=0$, z_M in the center of the $Pb_{1-x}Mn_xSe$ layer; 5, CB [111] valley, $n=0$, z_M in the center of the $Pb_{1-x}Mn_xSe$ layer; 6, CB [111] valley, $n=0$, z_M in the center of the $Pb_{1-x}Mn_xSe$ layer.

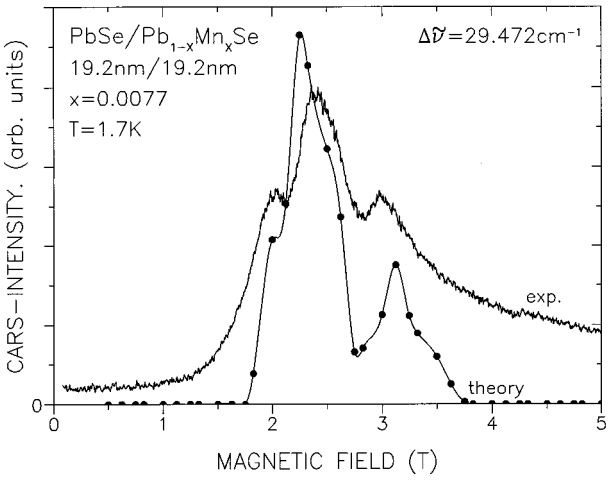

FIG. 16. Experimental recording of the CARS intensity vs magnetic field (—) and calculated line shape (only resonant part of the nonlinear susceptibility) (—●—). Sample: MQW No. 43, $T=1.7$ K, $\Delta\tilde{\nu}=29.472$ cm^{-1}.

V. CONCLUSIONS

A thorough experimental study of diluted magnetic PbSe/$Pb_{1-x}Mn_xSe$ structures grown by molecular-beam epitaxy has been presented involving magnetophotoluminescence, interband magneto-optical transitions, and coherent anti-Stokes Raman scattering. For comparison with theory, model calculations have been performed, based on an envelope-function calculation for the IV–VI compound band structure including the exchange interaction of the quasifree electrons and holes with the spins of the localized $3d$ electrons of the manganese ions in the mean-field approximation.

Apart from the band offset, no adjustable parameters were used in the calculations. All relevant band parameters were taken from experiments with PbSe and $Pb_{1-x}Mn_xSe$ epitaxial layers, the structural parameters of the PbSe/$Pb_{1-x}Mn_xSe$, SL's were determined by x-ray diffraction. The four exchange parameters for electrons and holes in $Pb_{1-x}Mn_xSe$ were obtained from CARS experiments on $Pb_{1-x}Mn_xSe$ epilayers.

All experimental data on the PbSe/$Pb_{1-x}Mn_xSe$ structures, from photoluminescence, interband-magnetoabsorption, and coherent anti-Stokes Raman scattering experiments, are consistent with a staggered band lineup in the PbSe/$Pb_{1-x}Mn_xSe$ system, in agreement with optical interband absorption data at $B=0$.[16] In the interband transitions, the initial and final states reside in spatially different layers. The staggered band lineup relaxes the $\Delta n=0$ interband selection rule, a feature that has been observed in interband magnetoabsorption, i.e., we have clearly identified transitions $n=1$ (valence band)$\rightarrow n=3$ (conduction band), extrapolating to 174 meV in Fig. 11(b) and $n=3$ (valence band)$\rightarrow n=1$ (conduction band), extrapolating to 190 meV in Fig. 11(b).

The CARS experiments, probing the g factors of electrons and holes separately, give conclusive evidence of an alignment with holes essentially confined in the PbSe layers and

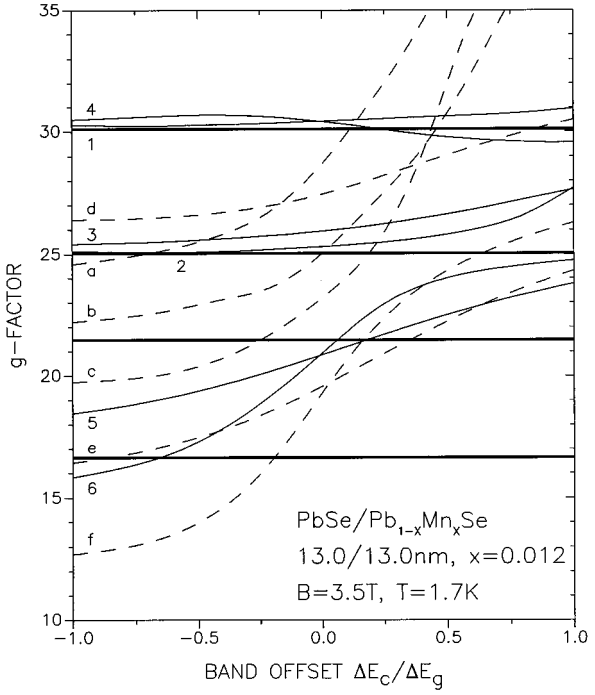

FIG. 17. Calculated g factors vs band offset at $B=3.5$ T and $T=1.7$ K for MQW sample No. 58. Full lines (1···6): center coordinates in $Pb_{1-x}Mn_xSe$ ($z_M=19.5$ nm). Dashed lines (a···f): center coordinates in PbSe ($z_M=6.5$ nm). Bold horizontal lines: experimental results. 1,a: VB, $n=1$, [11 1] valley; 2,b: VB, $n=1$, [111] valley; 3,c: VB, $n=1$, [111] valley; 4,d: CB, $n=0$, [11 1] valley; 5,e: CB, $n=0$, [111] valley; 6,f: CB, $n=0$, [111] valley.

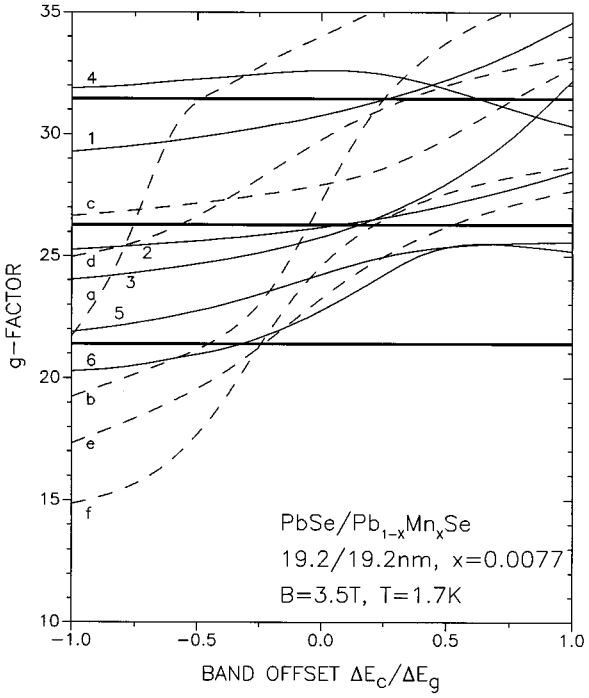

FIG. 18. Calculated g factors vs band offset at $B=3.5$ T and $T=1.7$ K for MQW sample No. 43. Full lines (1···6): center coordinates in $Pb_{1-x}Mn_xSe$ ($z_M=28.8$ nm). Dashed lines (a···f): center coordinates in PbSe ($z_M=9.6$ nm). Bold horizontal lines: experimental results. 1,a: VB, $n=1$, [11 1] valley; 2,b: VB, $n=1$, [111] valley; 3,c: VB, $n=1$, [111] valley; 4,d: CB, $n=0$, [11 1] valley; 5,e: CB, $n=0$, [111] valley; 6,f: CB, $n=0$, [111] valley.

electrons in the $Pb_{1-x}Mn_xSe$ layers and already a considerable leakage of the electron wave function into the barriers occurs. The band-structure calculations of the SL's confirm the observed small variation of the CARS resonance positions with increasing temperature for the normalized band offset of $\Delta E_c/\Delta E_g = -0.4$. All these CARS experiments are carried out in Voigt geometry, with the magnetic field oriented parallel to the layers, where the electric and magnetic motions are not decoupled, giving rise to position-dependent Landau energies.

An interesting feature is the rather large value of the nonresonant part of $\chi^{(3)}$ observed in the superlattices, a striking difference in comparison to the results on homogeneous $Pb_{1-x}Mn_xSe$. Also the resonant parts of $\chi^{(3)}$ in the SL's are substantially increased as compared to bulk material, leading to remarkably high intensities for rather small total thicknesses of the SL's.

In the magnetic-field range investigated, the band lineup stays staggered, i.e., there is no magnetic-field-induced transition to a type-I band alignment. Qualitatively, this can be understood because for the holes, essentially confined in diamagnetic layers, field-induced changes of the offset are rather negligible. For the electrons that are mainly in the $Pb_{1-x}Mn_xSe$ layers the exchange interaction is small.

A strong enhancement of the nonresonant part of the third-order nonlinear susceptibility has already been predicted for wide-gap semiconductor superlattices such as GaAs/AlGaAs. In the present work, this strong enhancement was demonstrated for narrow-gap superlattices. In addition, in superlattices also the resonant part of $\chi^{(3)}$ is substantially increased with respect to bulk material and thus a superlattice sample thickness of the order of 200 nm is sufficient for a reasonable signal-to-noise ratio. The series of investigations performed shows that spin-resonant optical four-wave mixing is indeed a very powerful tool for the investigation of diluted magnetic semiconductor superlattices.

ACKNOWLEDGMENTS

This work was supported by Deutsche Forschungsgemeinschaft, Bonn, by the FWF, Vienna and by Gesellschaft für Mikroelektronik, Austria.

[1] Z. Feit, D. Kostyk, R. J. Woods, and P. Mak, Appl. Phys. Lett. **58**, 343 (1991).
[2] M. Tacke, B. Spranger, A. Lambrecht, P. R. Norton, and H. Böttner, Appl. Phys. Lett. **53**, 2260 (1988).
[3] I. I. Zasavitskii, L. Kowalzcyk, B. N. Matsonashvili, and A. V. Sazonov, Fiz. Tekh. Poluprovodn. **22**, 2118 (1988) [Sov. Phys. Semicond. **22**, 1338 (1988)].
[4] K. H. Schlereth, B. Spranger, H. Böttner, A. Lambrecht, and M. Tacke, Infrared Phys. **30**, 449 (1990).
[5] D. L. Partin, IEEE J. Quantum Electron. **QE-24**, 1716 (1988).
[6] J. R. Anderson, G. Kido, Y. Nishina, M. Górska, L. Kowalczyk, and Z. Golacki, Phys. Rev. B **41**, 1014 (1990).
[7] M. Górska and J. R. Anderson, Phys. Rev. B **38**, 9120 (1988).
[8] W. Hofmann, U. Fichtel, H. Pascher, N. Frank, and G. Bauer, Phys. Rev. B **45**, 8742 (1992).
[9] G. Bauer, H. Pascher and W. Zawadzki, Semicond. Sci. Technol. **7**, 703 (1992).
[10] F. Geist, H. Pascher, N. Frank, and G. Bauer, Phys. Rev. B **53**, 3820 (1996).
[11] T. Dietl, C. Sliwa, G. Bauer, and H. Pascher, Phys. Rev. B **49**, 2230 (1994).
[12] L. Kowalczyk, Semicond. Sci. Technol. **6**, 115 (1991).
[13] H. Pascher, G. Bauer, and R. Grisar, Phys. Rev. B **38**, 3383 (1988).
[14] H. Pascher, Semicond. Sci. Technol. **5**, 141 (1990).
[15] N. Frank, A. Voiticek, H. Clemens, A. Holzinger, and G. Bauer, J. Cryst. Growth **126**, 293 (1993).
[16] S. Yuan, N. Frank, G. Bauer, and M. Kriechbaum, Phys. Rev. B **50**, 5286 (1994).
[17] H. Pascher, F. Geist, M. Kriechbaum, and N. Frank, Phys. Scr. T **45**, 214 (1992).
[18] N. Koguchi, S. Takahashi, and T. Kiyosawa, Jpn. J. Appl. Phys. **27**, 2376 (1988).
[19] H. Pascher, Appl. Phys. B **34**, 107 (1984).
[20] G. L. Eesley, *Coherent Raman Spectroscopy* (Pergamon, Oxford, 1981).
[21] W. Bloss and L. Friedmann, J. Vac. Sci. Technol. B **1**, 150 (1983).
[22] D. L. Mitchell and R. F. Wallis, Phys. Rev. **151**, 581 (1966).
[23] G. Bauer, in *Narrow Gap Semiconductors*, edited by W. Zawadzki, Lecture Notes in Physics Vol. 133 (Springer, Berlin, 1980), p. 427.
[24] M. Kriechbaum, *Two-Dimensional Systems: Physics and New Devices*, edited by G. Bauer, F. Kuchar, and H. Heinrich, Springer Series in Solid State Sciences Vol. 67 (Springer, Berlin, 1986), p. 120.
[25] M. Kriechbaum, P. Kocevar, H. Pascher, and G. Bauer, IEEE J. Quantum Electron. **QE-24**, 1727 (1988).
[26] R. R. Galazka and J. Kossut, in *Narrow Gap Semiconductors* (Ref. 23), p. 245.
[27] For reviews on the exchange interaction in diluted magnetic semiconductors, see *Semiconductors and Semimetals*, edited by J. K. Furdyna and J. Kossut (Academic, Boston, 1988), Vol. 25.
[28] J. A. Gaj, R. Planel, and G. Fishman, Solid State Commun. **29**, 435 (1979).
[29] R. Rupprecht and H. Pascher, Phys. Rev. B **50**, 16 931 (1994).